

# Binarity of a protostar affects the evolution of the disk and planets

<https://doi.org/10.1038/s41586-022-04659-4>

Received: 14 October 2021

Accepted: 16 March 2022

Published online: 23 May 2022

 Check for updates

Jes K. Jørgensen<sup>1</sup>✉, Rajika L. Kuruwita<sup>1</sup>, Daniel Harsono<sup>2,3</sup>, Troels Haugbølle<sup>1</sup>, Lars E. Kristensen<sup>1</sup> & Edwin A. Bergin<sup>4</sup>

Nearly half of all stars similar to our Sun are in binary or multiple systems<sup>1</sup>, which may affect the evolution of the stars and their protoplanetary disks during their earliest stages. NGC 1333-IRAS2A is a young, Class 0, low-mass protostellar system located in the Perseus molecular cloud<sup>2</sup>. It is known to drive two bipolar outflows that are almost perpendicular to each other on the sky<sup>3,4</sup> and is resolved into binary components, VLA1 and VLA2, through long wavelength continuum observations<sup>5</sup>. Here we report spatially and spectrally resolved observations of a range of molecular species. We compare these to detailed magnetohydrodynamic simulations: the comparisons show that inhomogeneous accretion onto the circumstellar disks occurs in episodic bursts, driving a wobbling jet. We conclude that binarity and multiplicity in general strongly affect the properties of the emerging stars, as well as the physical and chemical structures of the protoplanetary disks and therefore potentially any emerging planetary systems.

Using the Atacama Large Millimeter/Submillimeter Array (ALMA; for details, see the Methods section), we observed a range of molecular rotational transitions as well as thermal dust continuum emission down to scales of  $0.09'' \times 0.04''$  or  $27 \times 12$  AU (astronomical units), adopting a distance of 299 parsecs for NGC 1333 (ref. <sup>6</sup>). Whereas the resulting data highlight the chemical richness with a large number of lines from complex organics in the region<sup>7</sup> associated with the primary component, VLA1, the focus here is on the morphology and kinematics linked to the binarity of the system.

Figure 1 shows the continuum emission at 1.2 mm tracing the thermal radiation from dust grains. The most prominent emission is seen at the locations of the two components of the binary. The high sensitivity of ALMA also makes it possible to trace extended structures originating from VLA1 extending out to scales of about 1,000 AU. Any larger scale emission is probably resolved out by the interferometer's lack of sensitivity to extended emission. The orientation of the VLA1 disk known from longer wavelength observations<sup>8</sup> is also indicated in the figure. No signs of that disk are seen here, probably because of the dust in the surrounding envelope being optically thick.

The shocks associated with the bipolar jets driven by the two protostars are clearly traced by silicon monoxide emission (Extended Data Figs. 1, 2): a jet in the north–south direction driven by VLA1 and another in the east–west direction driven by VLA2. The observations thereby connect the jets unambiguously to the separate components of the binary. For both jets, a wiggling structure is seen on large scales as a possible indication of precessing motions<sup>8</sup>. Also, the emission in the north–south jet is highly clumpy, an indication of episodic events in connection with its launching<sup>9,10</sup>. In the blue-shifted, southern part of this jet, the material at the most extreme velocities is slightly downstream compared to the apex of the jet, indicating that material is decelerated as the shock progresses through the molecular cloud material.

Other molecular species trace a very different component of the protostellar environment with very compact emission centred on VLA1 (Fig. 2). Many of these species are expected to be present in the inner envelope where, in particular, deuterated water and complex organics are thought to sublime off grains when the temperature increases above 100 K (ref. <sup>11</sup>). All of these species show a characteristic quadrupolar velocity structure with two similar velocity gradients in the east–west direction but in the opposite directions north and south of the VLA1 disk. These complex kinematics are intriguing and provide direct information on the gas flow in the natal binary environment.

The observations represent a snapshot in time of the formation of a binary system. To interpret the observations, particularly the kinematic structure of the gas, we have carried out ab initio magnetohydrodynamic (MHD) simulations of forming wide binaries (Supplementary Videos 1–4). We use deep adaptive mesh refinement and a zoom-in technique<sup>12</sup> to reach a maximum resolution of 0.8 AU while simultaneously including boundary and initial conditions from a larger molecular cloud environment similar to Perseus. The parameters of each simulation and the resulting simulated binaries are summarized in Extended Data Table 1. The binary components form through core fragmentation, followed by inspiraling motions, dynamical friction and deposition of orbital angular momentum to the circumstellar gas, similar to what is seen in idealized models<sup>13</sup>. To use the models to put a physical context to the observed features, particularly the kinematic structure seen in the moment maps of different molecular tracers of the gas (Fig. 2), we systematically reconstructed moment maps for all snapshots in the simulation. We then identified epochs and projections that reproduce the quadrupole radial-velocity structure seen in the observations, that is, show similar differences between the red- and blue-shifted velocities ( $\pm 1 \text{ km s}^{-1}$ ) on similar spatial (50–100 AU) scales in the dense gas around the protostar. By identifying these epochs

<sup>1</sup>Niels Bohr Institute, University of Copenhagen, Copenhagen K., Denmark. <sup>2</sup>Institute of Astronomy and Astrophysics, Academia Sinica, Taipei, Taiwan, ROC. <sup>3</sup>Institute of Astronomy, Department of Physics, National Tsing Hua University, Hsinchu, Taiwan, ROC. <sup>4</sup>Department of Astronomy, University of Michigan, Ann Arbor, MI, USA. ✉e-mail: jeskj@nbi.ku.dk

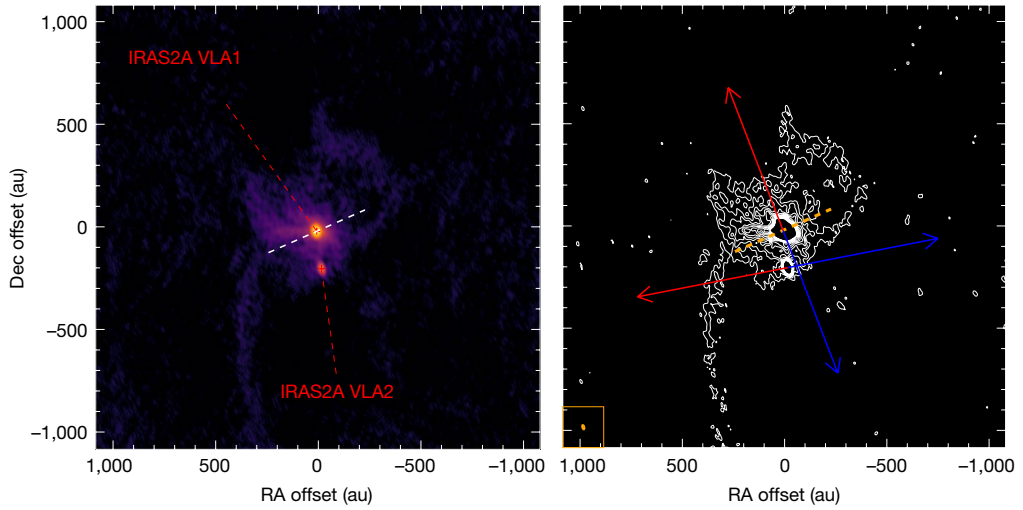


**Fig. 1 | Thermal dust continuum emission towards NGC 1333-IRAS2A.** Left, the 1.2 mm continuum emission shown as an image with the two sources and prominent and narrow extended structures. Right, the 1.2 mm continuum emission as contours in ten linearly spaced steps upwards from  $3\sigma$ . In the right panel, the arrows indicate the directions of the larger scale outflows from

previous CO observations<sup>5</sup>, and the ellipse in the bottom left corner indicates the beam of the observations. In both panels, the dashed line around NGC 1333-IRAS2A VLA1 indicates the orientation of the disk around that source from longer wavelength observations<sup>5</sup>.

in the simulations that match the observed features we could perform a non-parametric, unbiased, interpretation of the cause of the structures.

Extended Data Fig. 3 shows the selected matching moment maps. The simulated binaries are in the early evolutionary stage, with ages of 40,000–100,000 years. The velocity structure is dominated by

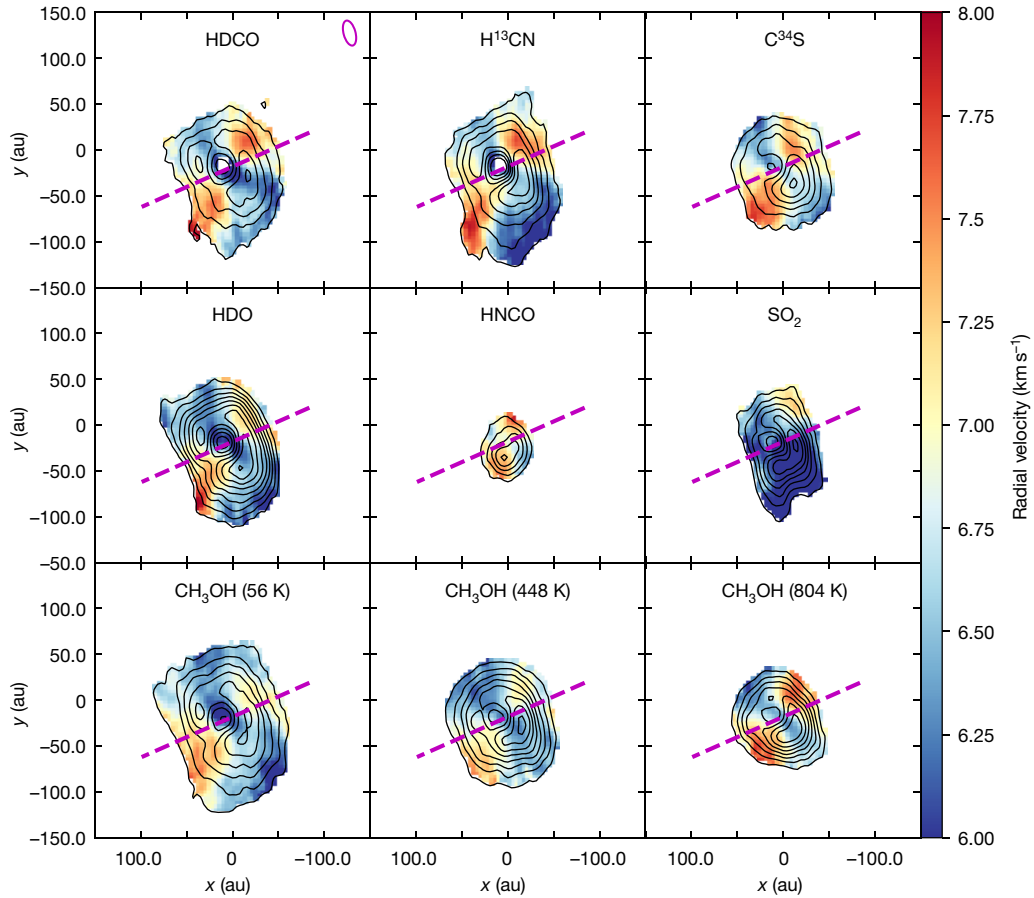


**Fig. 2 | Velocity maps of nine transitions of different molecules around VLA1.** In each panel, the moment-1 maps, shown as colour images, are calculated by integrating over velocities from 2 to 12  $\text{km s}^{-1}$  ( $\pm 5 \text{ km s}^{-1}$  relative to the systemic velocity) at positions where the integrated emission is above  $10\sigma$

(contours shown in steps of  $5\sigma$  above this). As in Fig. 1, the dashed lines indicate the orientation of the VLA1 disk<sup>5</sup>. The velocity scale from the moment-1 maps is indicated by the colour bar to the right.

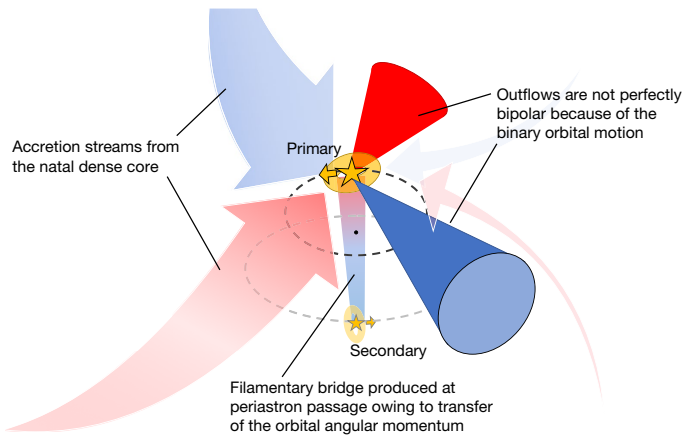
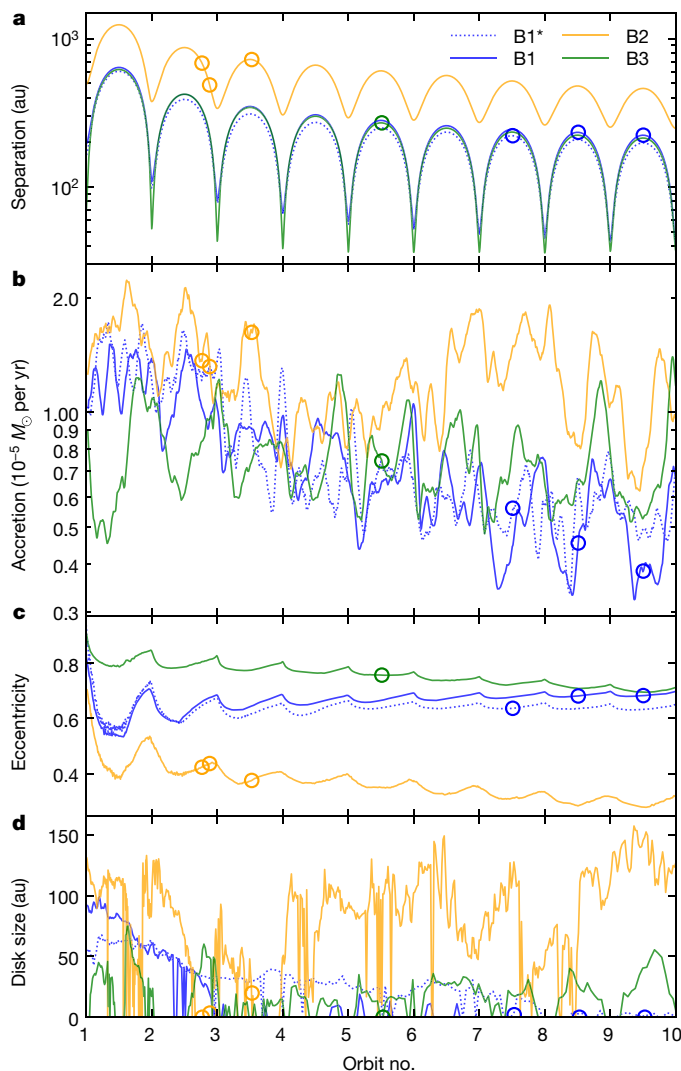


**Fig. 4 | Schematic figure showing the quadrupole radial-velocity structure.**

The primary is in the foreground and the secondary is in the background. Outflows produced by the primary star are not perfectly bipolar owing to the binary orbital motions. Accretion streams fall onto the binary from various directions, which in projection appear in the opposite direction to the outflows. The binary components entrain material when they pass at periastron, creating a sustained narrow bridge of gas and dust that connects the stars during their orbital motions.

the quadrupole radial-velocity structure seen in Fig. 2. The extended structures observed in the dust continuum emission also exist in the models, seen in the density projections (Extended Data Fig. 4 and videos in Supplementary Information), and correspond to accretion streamers feeding the protostars from the larger molecular cloud filament in which the cores are embedded<sup>15</sup>, coupled with asymmetric outflows due to binary orbital motion.

Besides the quadrupolar kinematic structure, many of the features from the simulations above are directly reflected in the observables: the bursts may lead to an increase of jet activity that are reflected in the shock knots observed on large scales towards the north–south outflow of VLA1. In later evolutionary stages, the cadence of these bursts follow the binary orbital time-scale, but in the earlier stages several events can be introduced per orbital period (Methods and Fig. 3). The misaligned jets are also a natural consequence of the formation of the wide binary; initially, the angular momentum vector of the forming disks reflect the alignment of the accretion streamers that fed them<sup>16</sup>. The subsequent dynamical evolution of the system will cause the binary components to migrate to smaller more stable and aligned orbits. Remnants of such misalignment can be seen on disk scales, for example, in binary systems with misaligned circumstellar and circumbinary disks<sup>17</sup>.

Figure 3 also illustrates the important role that the early evolution of a young binary system may play in determining the structure of its protoplanetary disks. The episodic bursts of accretion and associated increases in protostellar luminosity will cause molecules to sublime from icy grain mantles in extended regions around the central protostars and thereby shift the snow lines to larger radii<sup>18–20</sup>. The time-scale for freeze-out at the density and temperature characteristic of the envelope at 100 AU scales observed here is of the order of 1,000 years, similar to the binary orbital period and longer than the typical separation between the accretion bursts (Methods). Thus, there will be a close connection between the motions of the binary components and accretion in terms of sublimating the grains on large scales that possibly can lead to the formation of more complex species through gas-phase reactions<sup>21</sup>. Similarly, the regions where carbonaceous grains themselves may evaporate will be moved to larger radii: besides affecting the molecular composition in the immediate gas around the young star, this will also regulate the balance between refractory and volatile elements in these systems<sup>22</sup>. Finally, the disk size changes periodically

streamer-like infall and outflows, and the contributions from disks are small indicating that the disks were depleted recently. The complex quadrupole structure arises when an accretion event deposits a large amount of mass onto the circumstellar disk and outflows are launched. While the accretion changes rapidly, there is a broad modulation in the accretion rate over an orbit (Fig. 3). The higher eccentricity binaries with smaller separation (models B1 and B3) show pulsed accretion, with accretion rates peaking in the second half of an orbit (consistent with ref. <sup>14</sup>), and produces quadrupole radial-velocity structures near apastron after a few orbits, in which the kinematic structure is dominated by infall and corresponding outflows. The lower eccentricity binary with larger separation (model B2) also shows varying accretion, but in the first three orbits, the accretion rate peaks near apastron. In most instances in which a match was found, the binary is either developing or just past an accretion burst with related outflows that are dragged along the binary orbit. On the basis of an investigation of the 3D evolution of the systems, we made the schematic shown in Fig. 4. The schematic illustrates how accretion streams and outflows create

during an orbit. As there is some evidence that planet-formation has already started during the deeply embedded stages studied here, these effects may all be important components for determining the physical and chemical characteristics of the emerging planets.

## Online content

Any methods, additional references, Nature Research reporting summaries, source data, extended data, supplementary information, acknowledgements, peer review information; details of author contributions and competing interests; and statements of data and code availability are available at <https://doi.org/10.1038/s41586-022-04659-4>.

1. Duchêne, G. & Kraus, A. Stellar multiplicity. *Annu. Rev. Astron. Astrophys.* **51**, 269–310 (2013).
2. Jennings, R. E., Cameron, D. H. M., Cudlip, W. & Hirst, C. J. IRAS observations of NGC1333. *Mon. Not. R. Astron. Soc.* **226**, 461–471 (1987).
3. Sandell, G., Knee, L. B. G., Aspin, C., Robson, I. E. & Russell, A. P. G. A molecular jet and bow shock in the low mass protostellar binary NGC 1333-IRAS2. *Astron. Astrophys.* **285**, L1–L4 (1994).
4. Jørgensen, J. K., Hogerheijde, M. R., van Dishoeck, E. F., Blake, G. A. & Schöier, F. L. Outflows, rotation and chemistry on small scales in the protostellar system NGC1333-IRAS2. *Astron. Astrophys.* **413**, 993–1007 (2004).
5. Tobin, J. J. et al. The VLA Nascent Disk and Multiplicity (VANDAM) survey of Perseus protostars. resolving the sub-arcsecond binary system in NGC 1333 IRAS2A. *Astrophys. J.* **798**, 61 (2015).
6. Zucker, C. et al. Mapping distances across the perseus molecular cloud using CO observations, stellar photometry, and Gaia DR2 parallax measurements. *Astrophys. J.* **869**, 83 (2018).
7. Jørgensen, J. K. et al. Probing the inner 200 AU of low-mass protostars: high excitation transitions of organic molecules and continuum emission at high angular resolution toward the class 0 young stellar object NGC 1333-IRAS2A. *Astrophys. J.* **632**, 973 (2005).
8. Fendt, C. & Zinnecker, H. Possible bending mechanisms of protostellar jets. *Astron. Astrophys.* **334**, 750–755 (1998).
9. Frank, A. et al. In *Protostars and Planets VI* (eds. Beuther, H. et al.) 451 (Univ. Arizona Press, 2014).
10. Plunkett, A. L. et al. Episodic molecular outflow in the very young protostellar cluster Serpens South. *Nature* **527**, 70–73 (2015).
11. Jørgensen, J. K., Belloche, A. & Garrod, R. T. Astrochemistry during the formation of stars. *Annu. Rev. Astron. Astrophys.* **58**, 727–778 (2020).
12. Kuffmeier, M., Haugbølle, T. & Nordlund, Å. Zoom-in simulations of protoplanetary disks starting from GMC scales. *Astrophys. J.* **846**, 7 (2017).
13. Kuruwita, R. L. & Federrath, C. The role of turbulence during the formation of circumbinary discs. *Astron. Astrophys.* **486**, A59 (2019).
14. Kuruwita, R. L., Federrath, C. & Haugbølle, T. The dependence of episodic accretion on eccentricity during the formation of binary stars. *Astron. Astrophys.* **641**, A59 (2020).
15. Kuffmeier, M., Calcutt, H. & Kristensen, L. E. The bridge: a transient phenomenon of forming stellar multiples. Sequential formation of stellar companions in filaments around young protostars. *Astron. Astrophys.* **628**, A112 (2019).
16. Pineda, J. E. et al. A protostellar system fed by a streamer of 10,500 au length. *Nat. Astron.* **4**, 1158–1163 (2020).
17. Brinch, C., Jørgensen, J. K., Hogerheijde, M. R., Nelson, R. P. & Gressel, O. Misaligned disks in the binary protostar IRS 43. *Astrophys. J. Lett.* **830**, L16 (2016).
18. Lee, J.-E. Chemical evolution in VELLOs. *J. Korean Astron. Soc.* **40**, 83–89 (2007).
19. Visser, R. & Bergin, E. A. Fundamental aspects of episodic accretion chemistry explored with single-point models. *Astrophys. J. Lett.* **754**, L18 (2012).
20. Jørgensen, J. K., Visser, R., Williams, J. P. & Bergin, E. A. Molecule sublimation as a tracer of protostellar accretion. Evidence for accretion bursts from high angular resolution C<sup>18</sup>O images. *Astron. Astrophys.* **579**, A23 (2015).
21. Taquet, V., Wirström, E. S. & Charnley, S. B. Formation and recondensation of complex organic molecules during protostellar luminosity outbursts. *Astrophys. J.* **821**, 46 (2016).
22. van 't Hoff, M. L. R., Bergin, E. A., Jørgensen, J. K. & Blake, G. A. Carbon-grain sublimation: a new top-down component of protostellar chemistry. *Astrophys. J. Lett.* **897**, L38 (2020).

**Publisher's note** Springer Nature remains neutral with regard to jurisdictional claims in published maps and institutional affiliations.

© The Author(s), under exclusive licence to Springer Nature Limited 2022

## Methods

### ALMA observations and calibration

NGC 1333-IRAS2A (phase centre at  $\alpha_{J2000} = 03^{\text{h}}28^{\text{m}}55^{\text{s}}57$ ;  $\delta_{J2000} = 31^{\circ}14'37''.03$ ) was observed on 16 and 17 July 2019 with the ALMA during its Cycle 6 (project ID 2018.1.00427.S). The weather both days was good with precipitable water vapour of about 0.9 mm. At the time of the observations, 43 antennas were used in the array in its C43-8 configuration providing baselines of 92–8,547 m. The observations were set up to target a set of lines in six narrow-band spectral windows around 1.2 mm listed in Extended Data Table 2. The targeted transitions are known tracers of the warm gas close to the young stars where ices sublimate ( $\text{HDO}$ ,  $\text{CH}_3\text{OH}$ ), the dense infalling envelope ( $\text{H}^{13}\text{CN}$  and  $\text{H}^{13}\text{CO}^+$ ) and shocks ( $\text{SiO}$ ) (for example, ref.<sup>11</sup> and references therein). A seventh broad-band spectral window centred at 257 GHz was used to increase the continuum sensitivity.

The data were calibrated and imaged using CASA (v.5.6)<sup>23</sup>. The complex gains were calibrated using the quasar J0336+3218 while the quasar J0237+2848 was used as flux and bandpass calibrator. A self-calibration was performed using the aggregate of line-free channels in the seven spectral windows. A first round of phase-only self-calibration was done on the entire set of observations. Subsequently an iterative phase-only self-calibration was performed down to the integration time of 2.02 s. Each of the gain solutions was interpolated across the channels in the spectral windows. After the calibration, the data were imaged and cleaned using the CASA *tclean* task. The resulting synthesized beam sizes with Briggs weighting of 0.5 were roughly  $0.096'' \times 0.044''$  (slightly dependent on frequency) with a position angle of  $16^\circ$  and the noise level 1.3–1.6 mJy beam<sup>-1</sup> channel<sup>-1</sup> in 244.1 kHz (roughly 0.3 km s<sup>-1</sup>) channels.

### Identification of lines

In addition to the transitions listed in Extended Data Table 2, emissions from a range of other molecular lines were seen, predominantly from complex organic molecules. The individual transitions were identified by performing synthetic spectral fits; in those fits, the predicted spectra are calculated assuming local thermodynamical equilibrium and optically thin line emission. For fixed line widths, the line strengths then depend on the excitation temperature and column density of the considered species that in turn can be constrained by comparison to the observed spectra. For the purpose of this paper, it is sufficient to note that the lines shown in Fig. 2 were all selected to be spectrally well-isolated from other transitions. Many of the transitions (those of  $\text{CH}_3\text{OH}$  and  $\text{C}^{34}\text{S}$ , for example) show peak brightness temperatures of 50–120 K in one beam of VLA1, a further demonstration that they are probing the warm gas in the protostellar envelope.

### SiO and SO<sub>2</sub> channel maps

Extended Data Figs. 1 and 2 shows the channel maps for SiO 6–5: the precession is clearly noted, for example, with the shift of the apex of the emission in the blue-shifted part of the north–south outflow at velocities above the 20 km s<sup>-1</sup> range, the low velocity (less than 10 km s<sup>-1</sup>) panels for the red-shifted part of that outflow as well as in red-shifted part of the east–west outflow. The outflow knots seen at velocities above 25 km s<sup>-1</sup> for the blue-shifted lobe are indicative of the episodic ejection events. The launching of the blue-shifted part of the east–west jet is seen in the 20 to 28 km s<sup>-1</sup> velocity range (Extended Data Fig. 5). Channel maps for the SO<sub>2</sub> transition on Fig. 2 ( $2_{5,4}-4_{1,3}$  at 241.6158 GHz) is shown in Extended Data Fig. 6. This specific transition is sensitive to the molecular emission of the southern part of the VLA1 outflow in particular (although not to the same degree as the SiO transition), which causes its morphology to deviate from the quadrupolar structure seen in other tracers in Fig. 2.

### Time-scales: orbit, shocks and freeze-out

The binary orbital period can be estimated as  $t_{\text{orbit}} = 2\pi\sqrt{\frac{a^3}{G(M_1 + M_2)}}$  where  $a$  is the sum of the semi-major axes of the orbits of the two stars

and  $M_1$  and  $M_2$  are their masses. For the observed projected separation of 185 AU (0.62° at a distance of 299 pc)<sup>5</sup> and assuming two  $1 M_\odot$  stars in a circular orbit, the period is approximately 1,800 years (1,400–2,800 years if the mass of each of the binary components is varied from 2.0 to  $0.5 M_\odot$ ). We note that the masses of the individual components are still unconstrained: from the luminosity of the entire system ( $60 L_\odot$  based on the estimate from ref.<sup>24</sup> scaled to the Gaia distance adopted in this paper) the accretion rates inferred for Class 0 protostars based on the mass-luminosity relation for Class 0 sources of ref.<sup>25</sup> would indicate a total system mass of  $4 M_\odot$ , that is, corresponding to the upper boundary in the estimate above. Given its activity, it is not unlikely that the NGC 1333-IRAS2A accretion rate would be on the high side compared to this estimate, which would indicate a lower mass and thus still in the estimated range above. It should also be noted that adopting the projected separation in the above estimate will be a lower limit to the true physical separation, causing the orbital time-scale to be too low by a factor depending on the separation in the radial distances of VLA1 and VLA2 (a factor 1.7 if the distance in the radial direction corresponds to the projected separation, for example). Finally, for more eccentric orbits, the periods will differ and depend on the projection on the sky and where in the orbits the system is observed as seen in the specific examples of orbital time-scales from the system matches in the MHD simulations in Extended Data Table 1.

This orbital time-scale is an upper limit to the time-scales for the episodic accretion events; as shown in Fig. 3 at late evolutionary times, the accretion events start following the orbital time-scales while, in particular, in earlier times this happens at a higher cadence. Considering the SiO channel maps (Extended Data Fig. 2, for example), two prominent shocks are seen in the blue-shifted part of the outflow lobe at roughly 1.5–2° and 3.5–4° separation at velocities of 20–30 km s<sup>-1</sup>. Calculating the time-scale as  $t_{\text{shocks}} = \frac{l}{v \tan(i)}$  where the  $l$  is the projected separation between the shocks on the sky (1.5–2.5° – or 450–750 AU) along the jet axis,  $v$  the (radial) velocity from the SiO emission and  $i$  the inclination of the jet, leads to an estimate of the time-scale of 70–180 years assuming an inclination of 45° (the inclination is not well-constrained but from the aspect ratio of the centimetre-wavelength VLA1 disk as well as the outflow morphology indicates an inclination in the range of 25–65°, that is, neither edge- nor face-on, which adds a factor of 2 uncertainty on the time-scales). This time-scale may reflect both the accretion rate variations and inhomogeneities in the structure of the ambient environment of the sources.

For the above calculations of both the orbital and accretion time-scales it should be noted that the uncertainty in the distance estimate is an extra factor, in particular, when calculating the linear distances on the sky. The error on the adopted distance of 299 pc is quoted to be 5–6% (ref.<sup>6</sup>). A search of sources within 2° of NGC 1333-IRAS2A in the early Gaia Data Release 3 catalogue<sup>26</sup> gives an average distance of 291 pc with a standard deviation of 8%. These differences and uncertainties will be minor compared to the other uncertainties in the estimates discussed above.

The final relevant time-scale is the freeze-out time-scale for molecules at the observed spatial scales of the envelope. The freeze-out rate for a neutral molecule can be estimated from  $\lambda = 2.3 \times 10^{-18} \left(\frac{T}{m}\right)^{0.5} n_{\text{H}_2}$  (s<sup>-1</sup>) (for example, equation (3) in ref.<sup>27</sup>) where  $T$  is the temperature of the gas in kelvin,  $m$  the molecular weight of the molecule and  $n_{\text{H}_2}$  the molecular hydrogen density in cm<sup>-3</sup>. At the observed scales of the protostellar envelope outside the hot corino, the density is expected to be of the order of  $10^7$  cm<sup>-3</sup> and the temperature about 70 K (refs.<sup>28,29</sup>). Inserting those in the equation above for a molecule such as  $\text{CH}_3\text{OH}$ , leads to a freeze-out time-scale of roughly 930 years (710–1,100 years if the temperature is varied from 120 to 50 K as indicated by the brightness temperatures noted above). Thus, from this estimate and with the inferred accretion rate variations, the molecular ice–gas balance will be strongly affected by the binarity.

## MHD simulations of binaries

To understand the origin of the quadrupole structure in the moment maps shown in Fig. 2, we analysed simulations of binary star formation in a turbulent environment using an unbiased non-parametric approach. The simulations were run with the MHD code RAMSES<sup>30</sup>. The global setup is a  $3,000 M_{\odot}$  piece of a molecular cloud in a 4-parsec cubic periodic box with solenoidal turbulent driving resulting in a typical velocity dispersion of  $2 \text{ km s}^{-1}$ . The global model is identical to that described in detail in ref.<sup>31</sup>, but with double the linear resolution, reaching 25 AU globally. This global simulation produced 318 stars that form systems of many architectures (for example, single stars, binaries, multiples). From this simulation, we select three isolated protostellar cores forming wide binaries with separations that match the observed projected separations of NGC 1333-IRAS2A at some point in their evolution. We are thus not exploring the kinematical structures of, for example, binaries in more narrow orbits. The properties of the three systems B1, B2 and B3 are listed in Extended Data Table 1, including simulation parameters and characteristics of the binaries. The cores are resimulated at a resolution of 3.2 AU. B1 was also simulated at 0.8 AU (referred to as simulation ‘B1’) as a resolution study to determine whether the binary orbital evolution was converged. From Fig. 3, we do not see any notable variation in the binary properties between the 0.8 and 3.2 AU simulations. The simulations use a barotropic equation of state<sup>14</sup>, which adjusts the adiabatic index to account for radiation effects during the collapse of protostellar cores. We use a very generous refinement criteria of up to 64 cells per Jeans length at the highest resolutions inside a 10,000 AU distance of the primary star to properly resolve the intricate dynamical structure. The methodology of zoom-in runs is described elsewhere<sup>12</sup>.

From the zoom-in simulations we calculated the density-weighted radial-velocity structure from eight projection angles distributed evenly around the cone defined such that the projected separation of the simulated binary was always 200 AU, thus matching the separation on the sky of the sources in the observations, resulting in 70,000 projected moment maps. The moment maps assume that the emission is optically thin and consequently that the intensity is directly proportional to the column density. We searched by eye through the simulated maps for systems that show the same velocity difference between the red- and blue-shifted emission ( $\pm 1 \text{ km s}^{-1}$  compared to the system velocity) on similar spatial scales (50–100 AU) in the dense gas around the primary component as in the observations. From the initial search, 29, 35 and 10 matches were found for B1, B2 and B3, respectively. Caution should be taken when comparing the simulations to observations, and the number of matches is not a quantifier on how well a simulation produced the observations because each simulation ran for varying numbers of orbits, and some matches were qualitatively better than others. These initial matches were then ranked by how well they reproduced the observations, and we present the nine projections from seven epochs that were among those that best reproduced the observed quadrupole radial-velocity structure, shown in Extended Data Fig. 3. These comparisons allow us to identify at which orbital phase the systems reproduce the observations and quantify the physical structures, typical inclination angles and states of the systems. Videos for the four simulations depicting the column density and density-weighted velocity fields along three projections are available in the Supplementary Information (Supplementary Videos 1–4). Still frames at the match times from these videos are shown in Extended Data Fig. 4. The relevant system parameters are summarized in Extended Data Table 1.

Radiation feedback is not accounted for in our simulations; however, our equation of state adjusts the adiabatic index to capture the initial isothermal collapse, adiabatic heating, H<sub>2</sub> dissociation and second adiabatic collapse, that occur during protostellar collapse. Previous work on radiation feedback in low-mass star formation has typically found suppressed fragmentation in circumstellar disks<sup>32,33</sup>, and in cores in very dense regions<sup>34–36</sup>. Although our binaries form from core

fragmentation, their initial separations are very large (a few thousand astronomical units); therefore it is unlikely that radiation feedback would have suppressed the fragmentation that formed the binaries in our simulations. Radiation feedback may be enhanced during accretion bursts due to accretion luminosity, but even for high-mass star formation simulations, outflows are found to dominate feedback<sup>34,37,38</sup>, and we do not expect that the inclusion of radiation would notably change the orbital and dynamical evolution of the binaries and the circumbinary medium. However, it would be important to investigate radiation feedback to accurately compute the astrochemistry in the simulations.

This theoretical investigation only explored the conditions in which a quadrupole radial-velocity structure occurred in binaries such as NGC 1333-IRAS2A. Future work exploring a wider parameter space of binary physical and projected separations, as well as varying mass ranges, will better constrain what type of systems can produce this quadrupole structure and what prevents this phenomenon from arising.

## Reporting summary

Further information on research design is available in the Nature Research Reporting Summary linked to this paper.

## Data availability

The datasets generated and/or analysed during the current study are available in the ALMA archive, <https://almascience.nrao.edu/almadata/archive> and are also available from the corresponding author upon reasonable request.

## Code availability

The MHD and gravity solvers used in this study are closely related to the public RAMSES version available at <https://bitbucket.org/rteyssie/ramses>. The numerical methods, developed in Copenhagen, relevant for star formation are described in ref.<sup>31</sup>.

23. McMullin, J. P., Waters, B., Schiebel, D., Young, W. & Golap, K. CASA architecture and applications. In *Proc. Astronomical Data Analysis Software and Systems XVI* (eds Shaw, R. A., Hill, F. & Bell, D. J.) Vol. 376, Astronomical Society of the Pacific Conference Series, 127 (Astron. Soc. Pacific, 2007).
24. Karska, A. et al. The Herschel-PACS legacy of low-mass protostars: the properties of warm and hot gas components and their origin in far-UV illuminated shocks. *Astrophys. J. Suppl. Ser.* **235**, 30 (2018).
25. Artur de la Villarmois, E. et al. Physical and chemical fingerprint of protostellar disc formation. *Astron. Astrophys.* **626**, A71 (2019).
26. Bailer-Jones, C. A. L., Rybizki, J., Fouesneau, M., Demleitner, M. & Andrae, R. Estimating distances from parallaxes. V. Geometric and photogeometric distances to 1.47 billion stars in Gaia early data release 3. *Astron. J.* **161**, 147 (2021).
27. Rodgers, S. D. & Charnley, S. B. Chemical evolution in protostellar envelopes: cocoon chemistry. *Astrophys. J.* **585**, 355–371 (2003).
28. Jørgensen, J. K., Schönier, F. L. & van Dishoeck, E. F. Physical structure and CO abundance of low-mass protostellar envelopes. *Astron. Astrophys.* **389**, 908–930 (2002).
29. Kristensen, L. E. et al. Water in star-forming regions with Herschel (WISH). II. Evolution of 557 GHz  $1_{0,0}-1_{0,1}$  emission in low-mass protostars. *Astron. Astrophys.* **542**, A8 (2012).
30. Teyssier, R. Cosmological hydrodynamics with adaptive mesh refinement. A new high resolution code called RAMSES. *Astron. Astrophys.* **385**, 337–364 (2002).
31. Haugbølle, T., Padoan, P. & Nordlund, Å. The stellar IMF from isothermal MHD turbulence. *Astrophys. J.* **854**, 35 (2018).
32. Offner, S. S. R., Klein, R. I., McKee, C. F. & Krumholz, M. R. The effects of radiative transfer on low-mass star formation. *Astrophys. J.* **703**, 131–149 (2009).
33. Bate, M. R. Stellar, brown dwarf and multiple star properties from a radiation hydrodynamical simulation of star cluster formation. *Mon. Not. R. Astron. Soc.* **419**, 3115–3146 (2012).
34. Klein, R. I. Feedback effects in the high mass and low mass star formation. In *Proc. Numerical Modeling of Space Plasma Flows, Astronum-2009* (eds Pogorelov, N. V. et al.) Vol. 429, Astronomical Society of the Pacific Conference Series, 97 (Astron. Soc. Pacific, 2010).
35. Krumholz, M. R., Klein, R. I. & McKee, C. F. Radiation-hydrodynamic simulations of the formation of Orion-like star clusters. II. The initial mass function from winds, turbulence, and radiation. *Astrophys. J.* **754**, 71 (2012).
36. Hennebelle, P., Commerçon, B., Lee, Y.-N. & Chabrier, G. What is the role of stellar radiative feedback in setting the stellar mass spectrum? *Astrophys. J.* **904**, 194 (2020).
37. Tanaka, K. E. I., Tan, J. C., Zhang, Y. & Hosokawa, T. The impact of feedback in massive star formation. II. Lower star formation efficiency at lower metallicity. *Astrophys. J.* **861**, 68 (2018).

# Article

38. Kuiper, R. & Hosokawa, T. First hydrodynamics simulations of radiation forces and photoionization feedback in massive star formation. *Astron. Astrophys.* **616**, A101 (2018).

**Acknowledgements** This paper makes use of the following ALMA data: ADS/JAO.ALMA#2018.1.00427.S. ALMA is a partnership of the European Southern Observatory (ESO; representing its member states), National Science Federation (NSF; United States) and National Institutes of Natural Sciences (NINS; Japan), together with the National Research Council Canada (NRC; Canada), Ministry of Science and Technology and Academia Sinica Institute of Astronomy and Astrophysics (MOST and ASIAA; Taiwan) and Korea Astronomy and Space Science Institute (KASI; Republic of Korea), in cooperation with the Republic of Chile. The Joint ALMA Observatory is operated by ESO, Associated Universities Inc./National Radio Astronomy Observatory (AUI/NRAO) and the National Astronomical Observatory of Japan (NAOJ). We acknowledge the Partnership for Advanced Computing in Europe (PRACE) for awarding us access to Curie at GENCI@CEA, France. Resources at the University of Copenhagen high-performance computing centre were used to carry out the data analysis and part of the modelling. J.K.J. acknowledges support from the Independent Research Fund Denmark (grant number DFF0135-00123B). R.L.K. received funding from the European Union's Horizon 2020 research and innovation programme under the Marie Skłodowska-Curie grant agreement no. 847523 'INTERACTIONS'. D.H. acknowledges support from the EACOA Fellowship from the East Asian Core Observatories Association.

D.H. is supported by the Centre for Informatics and Computation in Astronomy (CICA) and grant number 110J035319 from the Ministry of Education of Taiwan. T.H. and R.L.K. acknowledge support from the Independent Research Fund Denmark through grant no. DFF8021-00350B. The research of L.E.K. is supported by a grant from VILLUM FONDEN (grant number 19127).

**Author contributions** J.K.J., L.E.K. and E.A.B. designed the ALMA proposal. D.H. and J.K.J. calibrated and analysed the resulting observations. R.L.K. and T.H. performed and analysed the MHD simulations. All authors contributed to the comparisons and discussions as well as the writing of the paper.

**Competing interests** The authors declare no competing interests.

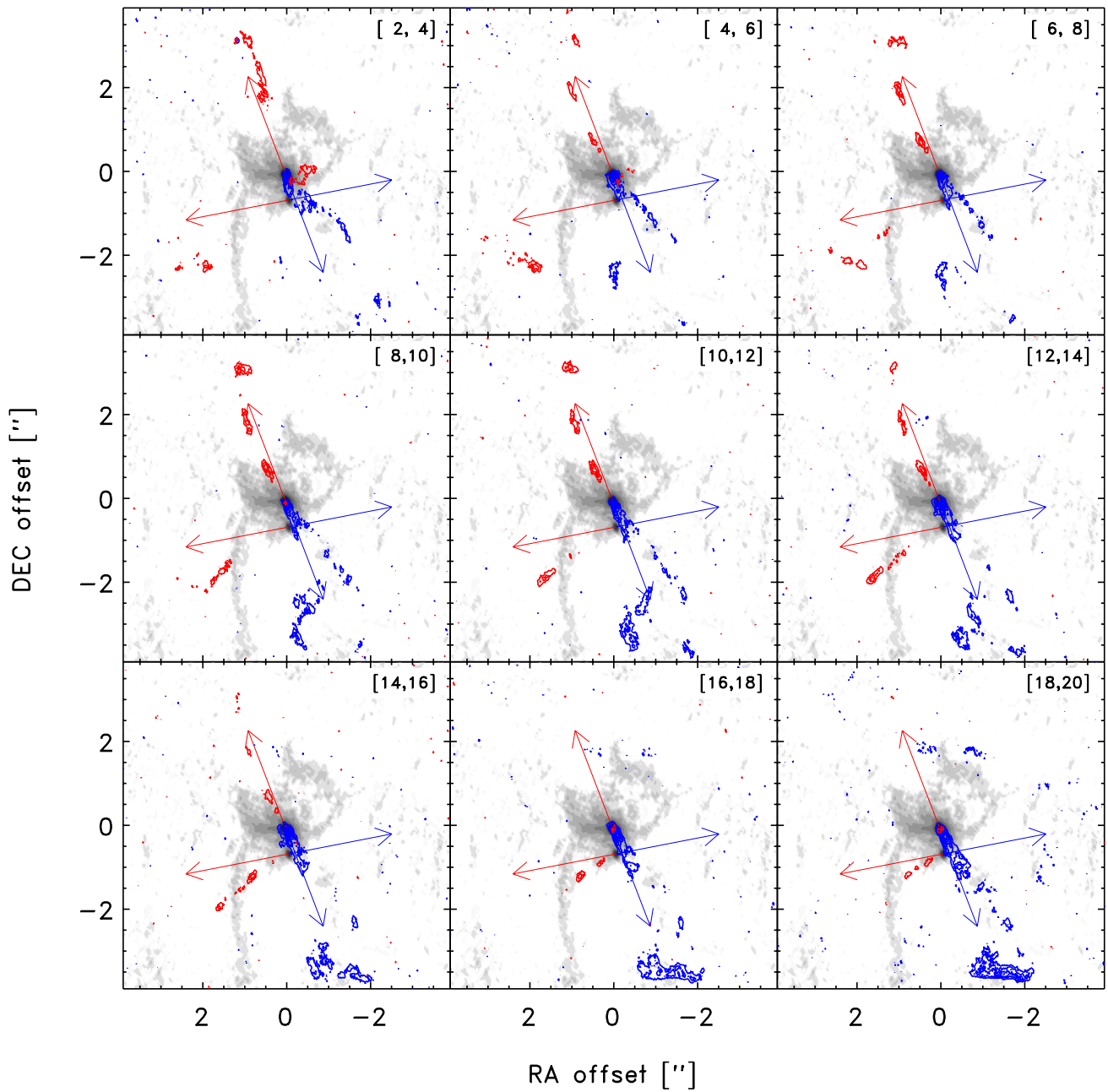
## Additional information

**Supplementary information** The online version contains supplementary material available at <https://doi.org/10.1038/s41586-022-04659-4>.

**Correspondence and requests for materials** should be addressed to Jes K. Jørgensen.

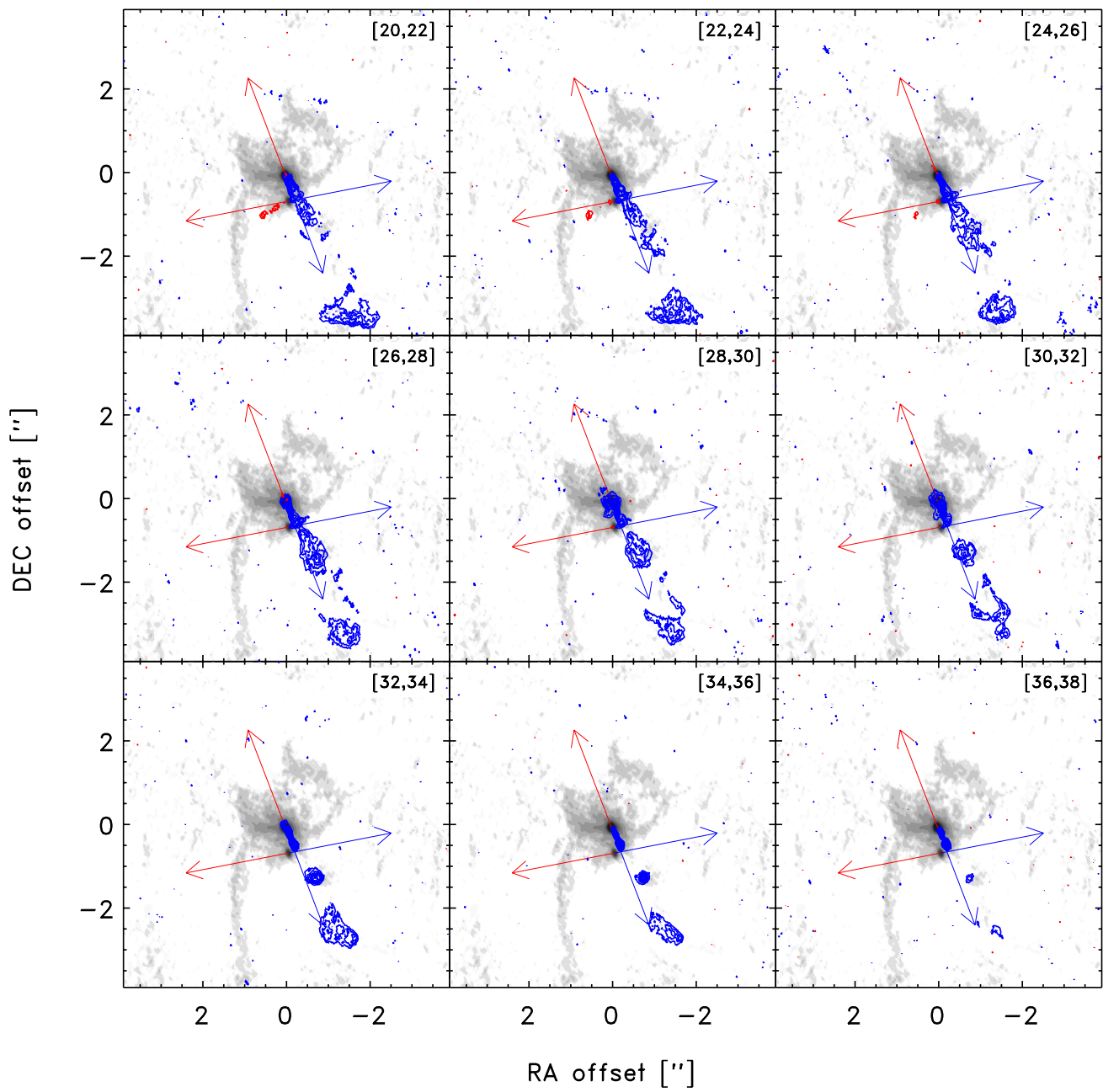
**Peer review information** *Nature* thanks Dominique Segura-Cox and the other, anonymous, reviewer for their contribution to the peer review of this work.

**Reprints and permissions information** is available at <http://www.nature.com/reprints>.

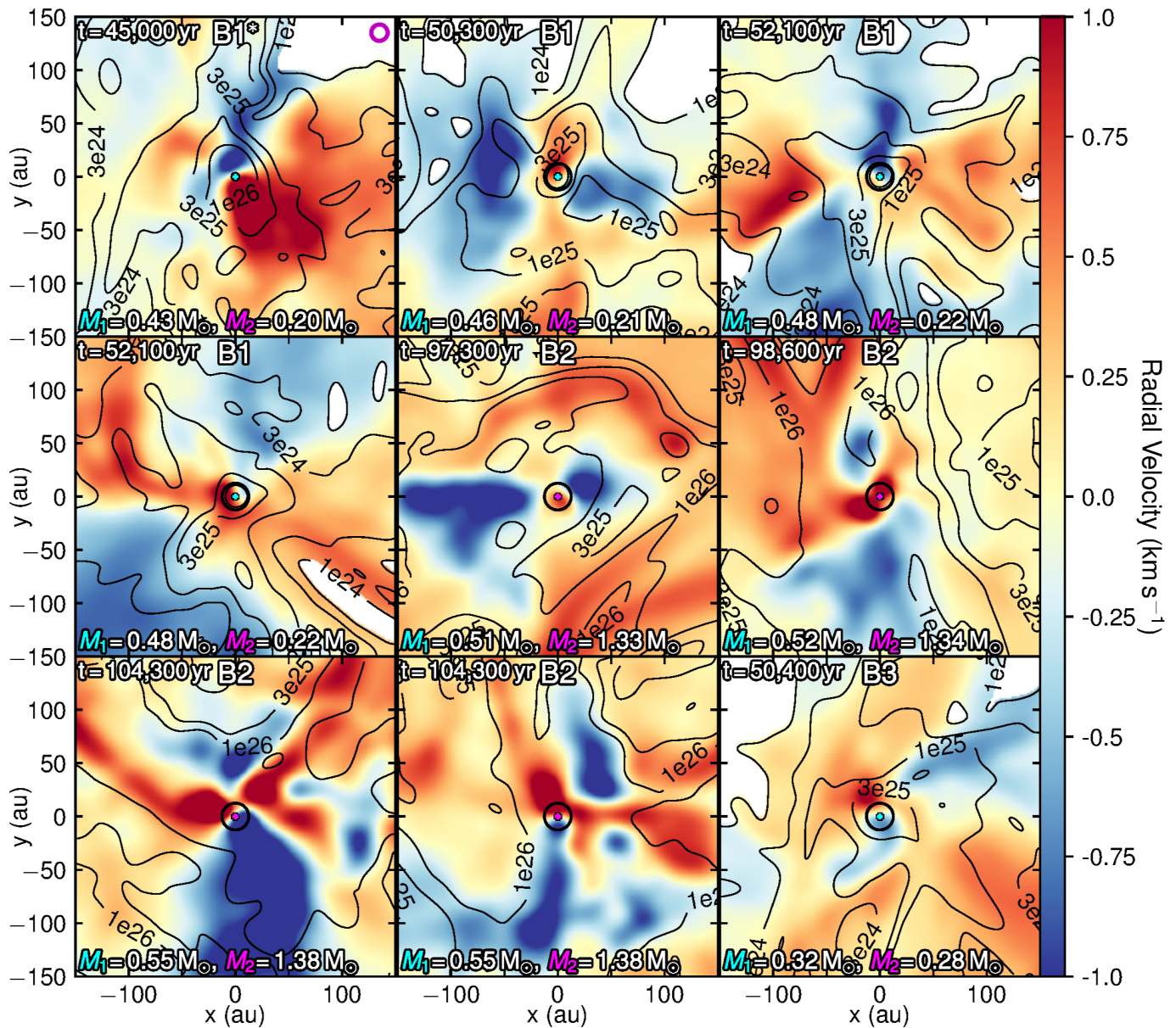


**Extended Data Fig. 1 | Channel maps of the silicon monoxide emission at low velocities.** Each panel shows the integrated emission over  $2 \text{ km s}^{-1}$  intervals given in the top right corners. The contours are given in steps of  $3\sigma$  in the

integrated maps. The directions of the two outflows and their polarity from previous CO observations<sup>5</sup> are indicated by the arrows. The dust continuum emission is seen as the greyscale background image.

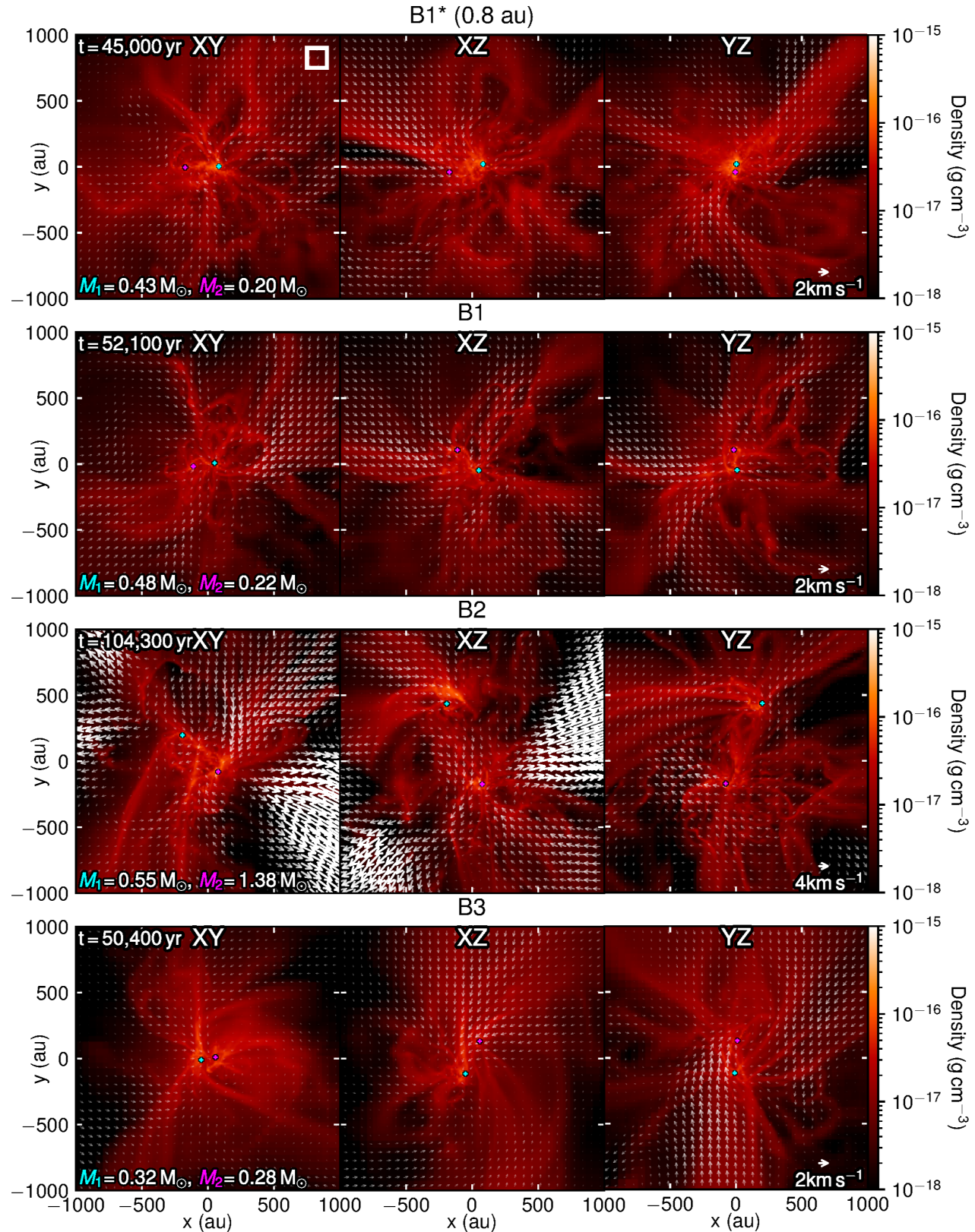


**Extended Data Fig. 2 | Channel maps of the silicon monoxide emission at high velocities.** As in Fig. 1 for high velocities from  $20$  to  $40 \text{ km s}^{-1}$  relative to the systemic velocity.



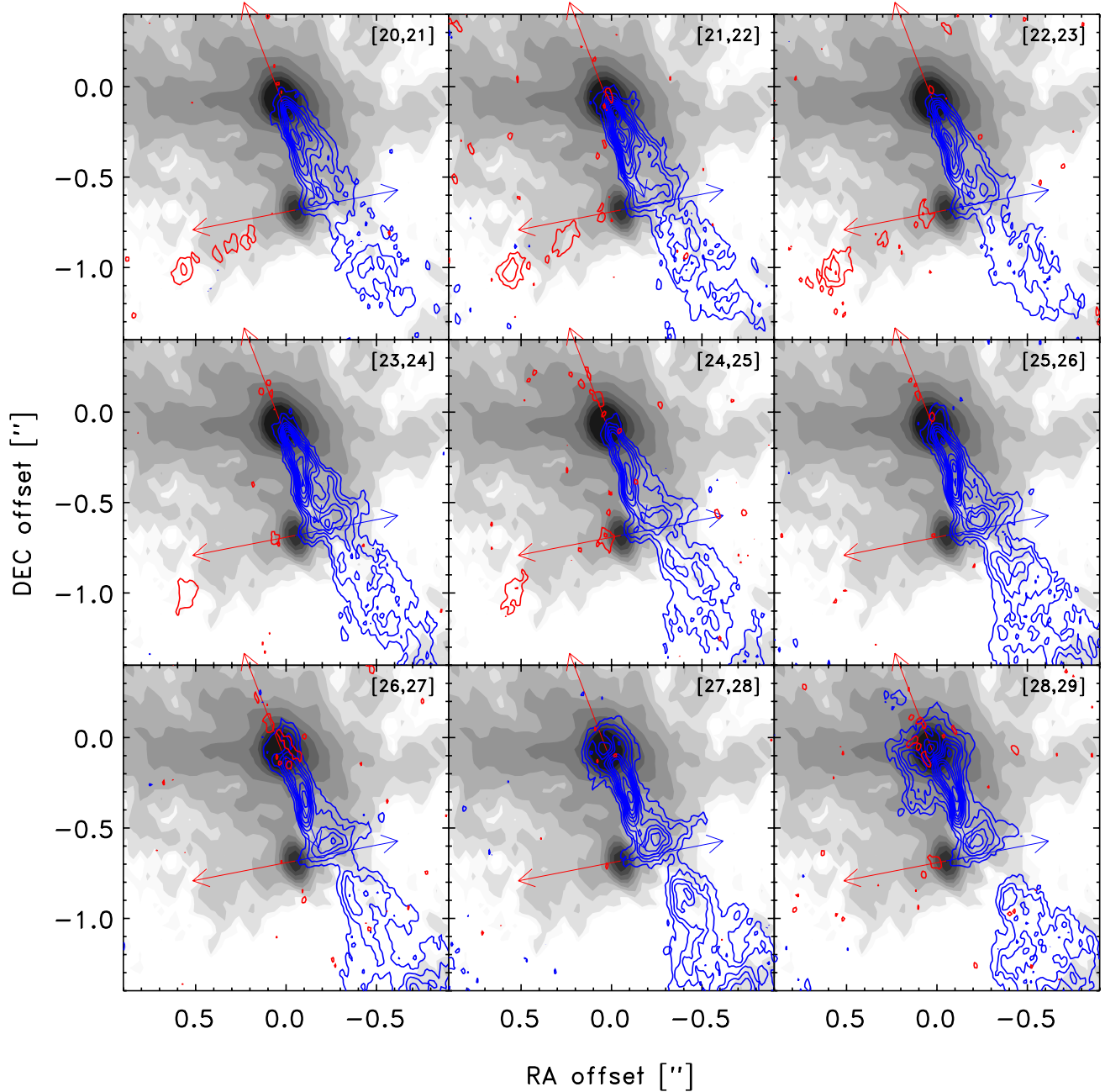
**Extended Data Fig. 3 | Simulated Velocity moment-1 maps.** The panels show the density-weighted radial velocity maps convolved with a Gaussian beam with a FWHM radius of 18 AU (annotated by the magenta circle in the top right of the first panel). This figure shows the nine best projections the quadrupole

radial velocity structure is reproduced. The contours annotate the column density integrated along the line of sight in logarithmically spaced bins from  $10^{24}$  to  $10^{27} \text{ cm}^{-2}$ .



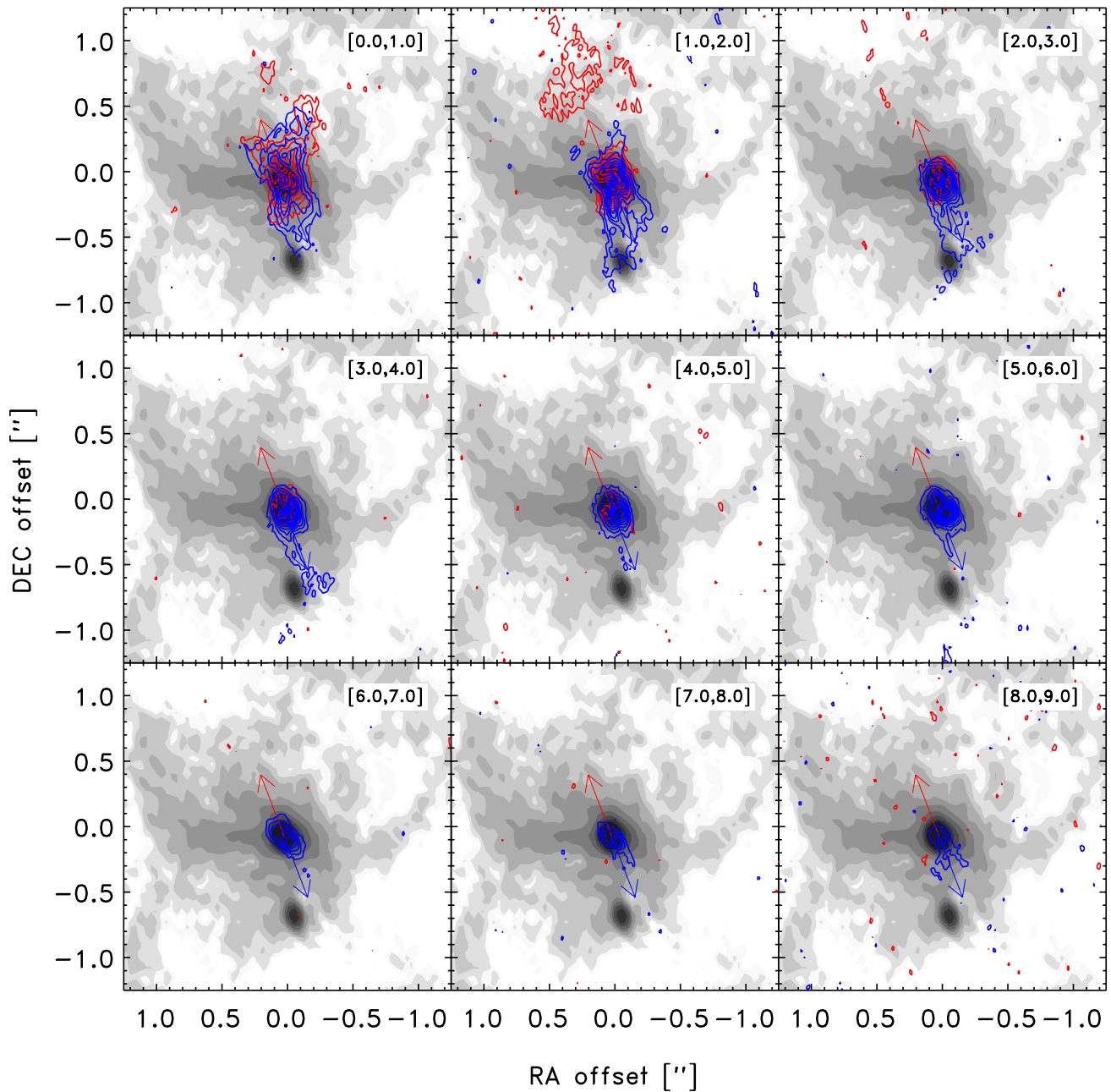
**Extended Data Fig. 4 | Density projections from simulations.** Projections along the x, y and z axis with a depth of 2,000 AU of density. The vector field annotates the density-weighted velocity. The selected times are when a

quadrupole RV structure was found around the primary component. The white box in the top left panel indicates the image size of the RV maps shown in Extended Data Fig. 3.



**Extended Data Fig. 5 | Silicon monoxide emission around VLA2.** As Extended Data Fig. 2 but zoomed-in at velocities between 20 and 30 km s<sup>-1</sup> in 1 km s<sup>-1</sup> intervals and on scales where the blue-shifted part of the jet from VLA2 can be seen.

# Article



**Extended Data Fig. 6 | Channel maps for sulfur dioxide emission.** As in Extended Data Figs. 1, 2 but illustrating the importance of the VLA1 outflow on the transition of sulfur dioxide (SO<sub>2</sub>) also shown in Fig. 2.

**Extended Data Table 1 | Model properties for snapshots used to match with observations**

Model	$t_1$ [kyr]	$t_2$	$M_1$ [ $M_\odot$ ]	$M_2$	$L_1$ [ $L_\odot$ ]	$L_2$	$\dot{M}_1$ [ $10^{-6} M_\odot \text{ yr}^{-1}$ ]	$\dot{M}_2$	$\dot{M}_{\text{tot}}$	$r_{\text{disk},1}$ [au]	$d_{\text{binary}}$ [au]	$P$ yr	$e$	$\Phi$ [deg]	$R_{\text{sim}}$ [au]	$i_{\text{sim}}$ [deg]
B1*	45	35	0.43	0.20	11.8	0.6	7.1	0.8	7.9	45	220	1900	0.64	182	0.8	65
B1	50	40	0.46	0.21	10.8	0.2	6.0	0.3	6.2	< 13	230	1900	0.68	182	3.2	59
	52	42	0.48	0.22	12.2	2.0	6.6	2.3	9.0	< 13	220	1800	0.68	180	3.2	64
B2	77	97	1.32	0.51	31.5	11.9	6.1	6.0	12.1	< 13	680	11300	0.42	268	3.2	17
	79	99	1.34	0.52	44.4	13.9	8.5	6.8	15.4	< 13	490	11100	0.44	314	3.2	24
	84	104	1.38	0.55	61.7	9.9	11.5	4.6	16.1	35	720	8700	0.37	183	3.2	16
B3	50	43	0.32	0.28	5.8	2.6	4.7	2.4	7.2	30	270	2500	0.76	183	3.2	48

$t_1$  and  $t_2$  are the ages of the primary and secondary stars.  $M_1$ ,  $M_2$  and  $L_1$ ,  $L_2$  are the masses and luminosities of the primary and secondary, respectively.  $\dot{M}_1$ ,  $\dot{M}_2$  and  $\dot{M}_{\text{tot}}$  are the accretion rates for the primary, secondary, and in total.  $r_{\text{disk},1}$  and  $d_{\text{binary}}$  represent the size of the disk around the primary component and the binary separation, respectively. A disk size of less than 13 au < 13 au means that the radial disk size was measured to be less than 4 cells.  $P$  and  $e$  are the period and eccentricity respectively of the orbit.  $\Phi$  is the phase of the orbit with respect to latest periastron.  $R_{\text{sim}}$  is the numerical resolution of the simulation while  $i_{\text{sim}}$  is the inclination between the simulated point of view and the binary orbit where an edge on view corresponds to 0 degrees.

# Article

## Extended Data Table 2 | Spectral setups

SPW	Frequency range	Target
0	256.080–257.940 GHz	Continuum
1	258.948–259.064 GHz	H <sup>13</sup> CN 3 – 2
2	260.191–260.308 GHz	H <sup>13</sup> CO <sup>+</sup> 3 – 2
3	260.394–260.628 GHz	SiO 6 – 5
4	240.960–241.429 GHz	CH <sub>3</sub> OH 5 <sub>k</sub> – 4 <sub>k</sub> , v <sub>t</sub> = 1
5	241.678–241.911 GHz	CH <sub>3</sub> OH 5 <sub>k</sub> – 4 <sub>k</sub> , v <sub>t</sub> = 0
6	241.439–241.673 GHz	HDO 2 <sub>1,1</sub> – 2 <sub>1,2</sub>

Corresponding author(s): Jes K. Jørgensen

Last updated by author(s): Feb 26, 2022

## Reporting Summary

Nature Portfolio wishes to improve the reproducibility of the work that we publish. This form provides structure for consistency and transparency in reporting. For further information on Nature Portfolio policies, see our [Editorial Policies](#) and the [Editorial Policy Checklist](#).

### Statistics

For all statistical analyses, confirm that the following items are present in the figure legend, table legend, main text, or Methods section.

n/a Confirmed

- The exact sample size ( $n$ ) for each experimental group/condition, given as a discrete number and unit of measurement
- A statement on whether measurements were taken from distinct samples or whether the same sample was measured repeatedly
- The statistical test(s) used AND whether they are one- or two-sided  
*Only common tests should be described solely by name; describe more complex techniques in the Methods section.*
- A description of all covariates tested
- A description of any assumptions or corrections, such as tests of normality and adjustment for multiple comparisons
- A full description of the statistical parameters including central tendency (e.g. means) or other basic estimates (e.g. regression coefficient) AND variation (e.g. standard deviation) or associated estimates of uncertainty (e.g. confidence intervals)
- For null hypothesis testing, the test statistic (e.g.  $F$ ,  $t$ ,  $r$ ) with confidence intervals, effect sizes, degrees of freedom and  $P$  value noted  
*Give P values as exact values whenever suitable.*
- For Bayesian analysis, information on the choice of priors and Markov chain Monte Carlo settings
- For hierarchical and complex designs, identification of the appropriate level for tests and full reporting of outcomes
- Estimates of effect sizes (e.g. Cohen's  $d$ , Pearson's  $r$ ), indicating how they were calculated

*Our web collection on [statistics for biologists](#) contains articles on many of the points above.*

### Software and code

Policy information about [availability of computer code](#)

Data collection

The MHD and gravity solvers used in this study are closely related to the public RAMSES version available at <https://bitbucket.org/rteyssie/ramses>. The numerical methods, developed in Copenhagen, relevant for star formation are described in Haugbølle et al. (2018, *Astrophys. J.* 854, 35)

Data analysis

The ALMA data were calibrated and imaged using the Common Astronomy Software Applications package, CASA (version 5.6). CASA is publicly available at <https://casa.nrao.edu/index.shtml>

For manuscripts utilizing custom algorithms or software that are central to the research but not yet described in published literature, software must be made available to editors and reviewers. We strongly encourage code deposition in a community repository (e.g. GitHub). See the Nature Portfolio [guidelines for submitting code & software](#) for further information.

### Data

Policy information about [availability of data](#)

All manuscripts must include a [data availability statement](#). This statement should provide the following information, where applicable:

- Accession codes, unique identifiers, or web links for publicly available datasets
- A description of any restrictions on data availability
- For clinical datasets or third party data, please ensure that the statement adheres to our [policy](#)

The paper utilised the ALMA data: ADS/JAO.ALMA#2018.1.00427.S. The ALMA data are available through the ALMA archive at <https://almascience.nrao.edu/alma-data/archive> and also from the corresponding author upon reasonable request.

# Field-specific reporting

Please select the one below that is the best fit for your research. If you are not sure, read the appropriate sections before making your selection.

Life sciences       Behavioural & social sciences       Ecological, evolutionary & environmental sciences

For a reference copy of the document with all sections, see [nature.com/documents/nr-reporting-summary-flat.pdf](https://nature.com/documents/nr-reporting-summary-flat.pdf)

## Life sciences study design

All studies must disclose on these points even when the disclosure is negative.

Sample size	The study concerns one protostellar binary system observed by ALMA based on previous data. Thus, the sample size was not a consideration.
Data exclusions	No data were excluded from the analysis.
Replication	Not relevant for the type of analysis.
Randomization	Not relevant for the type of analysis.
Blinding	Not relevant for the type of analysis.

## Reporting for specific materials, systems and methods

We require information from authors about some types of materials, experimental systems and methods used in many studies. Here, indicate whether each material, system or method listed is relevant to your study. If you are not sure if a list item applies to your research, read the appropriate section before selecting a response.

Materials & experimental systems		Methods	
n/a	Involved in the study	n/a	Involved in the study
<input checked="" type="checkbox"/>	<input type="checkbox"/> Antibodies	<input checked="" type="checkbox"/>	<input type="checkbox"/> ChIP-seq
<input checked="" type="checkbox"/>	<input type="checkbox"/> Eukaryotic cell lines	<input checked="" type="checkbox"/>	<input type="checkbox"/> Flow cytometry
<input checked="" type="checkbox"/>	<input type="checkbox"/> Palaeontology and archaeology	<input checked="" type="checkbox"/>	<input type="checkbox"/> MRI-based neuroimaging
<input checked="" type="checkbox"/>	<input type="checkbox"/> Animals and other organisms		
<input checked="" type="checkbox"/>	<input type="checkbox"/> Human research participants		
<input checked="" type="checkbox"/>	<input type="checkbox"/> Clinical data		
<input checked="" type="checkbox"/>	<input type="checkbox"/> Dual use research of concern		